Granular flows : fluidization and anisotropy

Wortel, G.H.

Chapter 4

A Nontrivial Critical Point in Granular Flows

4.1 Introduction

In this chapter we investigate the transition between slow and fast granular flows in the weakly vibrated split-bottom geometry. As we have seen in chapter 2, this transition is hysteretic in stress-controlled experiments at low vibration strength Γ.

To see how the transition develops with increasing Γ, we show a collection of flow curves in Fig. 4.1. The red curves on top correspond to low Γ, and the negative slope part around $\Omega = 0.1$ rps reflects the hysteretic regime. With increasing Γ, the magnitude of the hysteresis decreases. For $\Gamma_c \approx 0.43$, the flow curve no longer has a negatively sloped part, but instead contains an essentially flat part. At this plateau, there is a large range in Ω that corresponds to a very narrow range in torque around the critical torque T_c. For $\Gamma > \Gamma_c$, the flow curves are monotonic.

In this chapter we will explore the idea that (Γ_c, T_c) is similar to a second-order critical point. If we identify the flow curves with the variation of an order parameter ($\log(\Omega)$) as a function of two control parameters (T, Γ), then these curves are analogous to the well-known (P, V) curves for the gas-liquid transition, which are given by the van der Waals equation [100]. Water can be turned into vapor via a first order phase transition by decreasing the pressure P at low temperatures. Here, the order parameter which distinguishes the fluid phase from the gaseous phase is the volume V. At a certain higher temperature T_c, the transition becomes continuous at the second-order critical point (T_c, P_c). To make our analogy concrete, we associate the temperature with the vibration amplitude

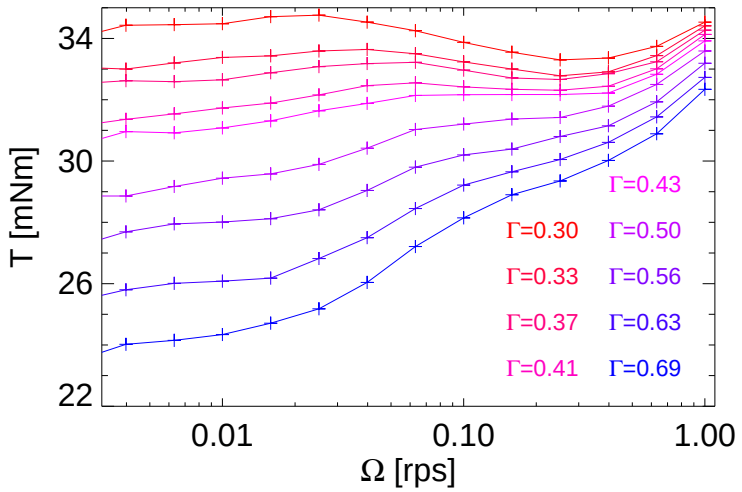

FIGURE 4.1: Examples of flow curves for different Γ. In the crossover between the curves with a negative slope part (red) and the monotonic ones (blue), there is a curve for $\Gamma \approx 0.43$ with an essentially horizontal plateau.

Vibrheology	Gas-Liquid	Ising Model
Vibration Γ	Temperature T	Temperature T
Torque T	Inv. Pressure P^{-1}	Inv. Magnetic Field H^{-1}
Flow rate Ω	Volume V	Inv. Magnetization M^{-1}

TABLE 4.1: Comparison of the control and order parameters between our system, the gas-liquid transition, and the Ising model.

Γ, the inverse pressure with the torque T and the inverse volume with the rotation rate Ω [1]. At low Γ, there is a discontinuous transition from slow to fast flow as T is increased. By choosing the correct combination (T_c, Γ_c), our flow transition becomes continuous. In Table 4.1, we summarize the mapping between our system and the gas-liquid transition, as well as the comparison to the Ising model [101, 102]. At this point, this is a purely an analogy.

[1] We denote the rotation rate with Ω if it concerns a control parameter or a time averaged value and with ω if it is a time-dependent order parameter.

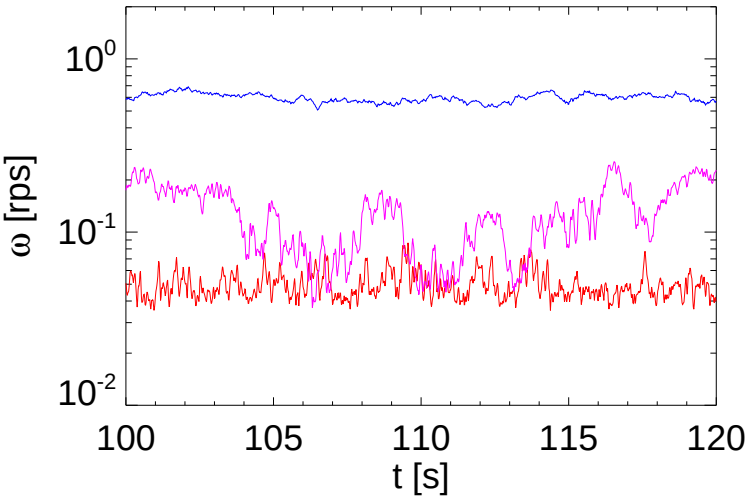

FIGURE 4.2: Three $\omega(t)$ signals for Γ just above Γ_c for $T < T_c$ ($\Gamma = 0.71$, $T = 30.1$ mNm, red), $T \approx T_c$ ($\Gamma = 0.71$, $T = 31.0$ mNm, pink) and $T > T_c$ ($\Gamma = 0.71$, $T = 31.6$ mNm, blue). The fluctuations are largest for the data set closest to the critical point.

To explore if the analogy to a critical point in our system is more than just a superficial coincidence, we will perform several experiments, both in rate and stress control.

First, we measure the flow curves $T(\Omega)$ in rate control. We study in detail how the shape of the flow curves changes as we vary Γ. We will consider: (a) the scaling of the distance between the local minimum and maximum of the flow curves for $\Gamma < \Gamma_c$, that decreases when approaching Γ_c, and (b) the scaling of the slope at the inflection point, which goes to zero when approaching Γ_c either from above or below. We will find that the shape of the flow curves can very well be described using a mean field picture [103, 104], and the critical exponents we extract from the data are equal to the mean field values within error bars.

Second, in stress control we study the fluctuations in $\omega(t)$. If we impose $\Gamma^* \equiv (\Gamma - \Gamma_c)/\Gamma_c \approx 0$ and $T^* \equiv (T - T_c)/T_c \approx 0$ - which corresponds to the plateau in Fig. 4.1 - we expect to see large fluctuations in ω. Moving away from the critical point, the flow curve gets steeper and we expect smaller fluctuations in ω. Indeed, we will provide evidence for such a variation of the fluctuations.

In general, the packing can be thought of to possess an effective viscosity η, so that $\omega = T/\eta(T)$. T is constant in experiments where we probe the fluctuations in the flow rate, but the packing (and thus η) continuously fluctuate. At the *flat* part of the flow curve, a tiny increase in T then leads to a large increase in ω, which in turn corresponds to a large change in η. If the flow curve is *steep*, a change in ω requires a large change in T. Based on this reasoning, we expect the magnitude of the fluctuations σ to be related to the slope of the flow curve via:

$$\sigma \sim \frac{1}{\partial T/\partial \Omega} \,. \tag{4.1}$$

For each Γ, we thus expect the fluctuations to be maximal at the inflection point (Ω_i, T_i) of the flow curve, where the slope is smallest. We have explored Eq. 4.1 in detail and found that, indeed, the fluctuations increase monotonically as the slope of $T(\Omega)$ gets flatter, but the prefactor depends on Γ and is different for the slow and fast flowing branch [105].

In Fig. 4.2, we show three $\omega(t)$ curves for Γ just above Γ_c and $T < T_i$, $T \approx T_i$ and $T > T_i$. We see that the fluctuations are non-monotonic in T and are largest around T_i. We will find that, in general, the fluctuations increase if the critical point is approached either by changing T or Γ; the corresponding critical exponent matches the mean field value.

Third, we study the characteristic time scale of the $\omega(t)$ signals via their autocorrelation function. Whereas the lower curve in Fig. 4.2 fluctuates rapidly with a time scale significantly below 1 s, there is a longer time scale in the critical curve. We will find that the time scale increases if the critical point is approached either by changing T or Γ. Even though a precise single time scale is hard to identify, we conclude that the critical exponent for the divergence of the characteristic time scale deviates from the mean field value.

The outline of this chapter is as follows: in Sec. 4.2 we will explain in more detail how we perform the experiments, and in Sec. 4.3 we will explicitly introduce the scaling relations and exponents that we test in our system. In Sec. 4.4 we discuss the scaling of the flow curves, and in Sec. 4.5 we consider the magnitude and time scale of the fluctuations that are measured in stress control. We finish with an appendix, where we suggest a simple heuristic model to describe the flow in App. 4.A.3.

4.2 Setup and Protocol

To perform the measurements, we have developed an extended version of the setup that was introduced in Sec. 2.2. Our geometry has the complication that, because of the flexure, the angle θ of the disk that drives the system is not necessarily the same as the angle measured by the rheometer. In the case of experiments at constant Ω, we are not significantly hindered by this problem as we measure flow in *steady state*, where the deflection of the flexure also reaches a steady state value. For stress-controlled *fluctuation* measurements, the deflection of the flexure will vary, and the motion above and below the flexure will definitely not be the same. To circumvent this, we extended the setup by mounting an optical encoder just below the flexure - see Fig. 4.3 - which is thus rigidly connected to the disk.

In most encoders there is mechanical contact between the sensor and the rotating axis which results in a torque similar to the torques we want to measure. We therefore have specifically chosen an encoder in which there is no contact between these two parts.

The encoder (Heidenhain ERO 1285 - 2500) consists of a glass disk with 2500 engraved lines which is mounted on the axis of the system. Above the disk - attached to the cell itself and not to the axis - there is an LED and below the disk there are sensors that detect how much light shines through the disk. If there is a line between LED and detector, the sensor measures a lower light intensity. The light intensity is turned into a voltage, which is the raw output of the device.

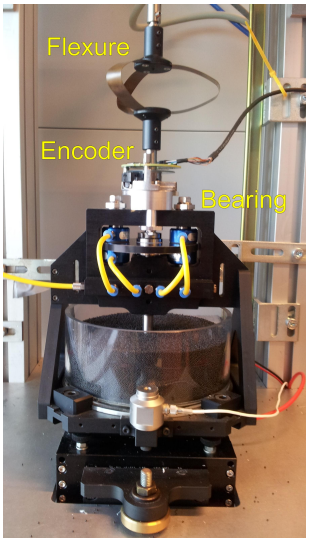

FIGURE 4.3: A photo of the shear cell with the new angular encoder.

The disadvantage of a non-contact encoder is that it has to be mounted very accurately. The distance between the sensor and the engraved disk is crucial and has to be 0.2 ± 0.03 mm and may not vary much over a full rotation of the disk. To achieve this, we had to realign the entire setup and renew the driving axis. The aligning is done by reading out the

raw sine signal of the encoder and by adjusting the alignment such that amplitude of the signal does not vary with θ.

In case of a constant rotation rate, the output of the encoder has the shape of a sine wave with constant frequency. We use an interpolator (Heidenhain IBV 101) which extracts from each sine wave a series of 10 block pulses. This increases our resolution by a factor 10. There are two channels that measure the light through different spots of the disk, which is required to determine the direction of the rotation. We connect the two pulse signals we obtain from the interpolator to the counter ports on the DAQ I/O card, which can count pulses with frequencies up to 80 MHz. From the two pulse trains, θ can be calculated via a standard method called "quadrature encoding" [106], which as a bonus gives an additional factor 4 in resolution (resulting in $2500 \times 10 \times 4 = 10^5$ pulses per rotation).

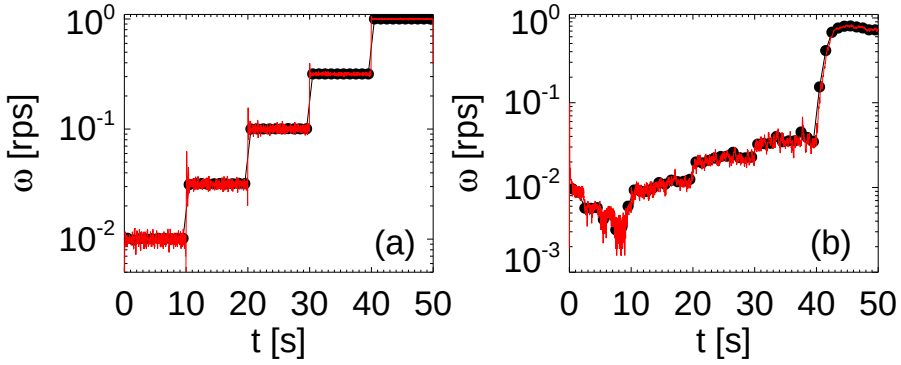

FIGURE 4.4: Comparison between ω measured by the rheometer (black) and the encoder (red). In (a), we control Ω at 5 different values, each for 10 s, in (b) we control T, also at 5 values, for 10 s. The encoder signal resolves more fluctuations because it measures the disk's angle at much higher temporal resolution. For the encoder signal we measure the position of the disk using a temporal resolution of 63 Hz and obtain ω by taking a three-point derivative. The good correspondence between the red and black data shows that the encoder works well in the Ω range where we will measure.

The accuracy of an encoder depends on how constant the distance between the engraved lines on the disk is. An estimate for the accuracy is 10% of the grading, which in our case leads to 0.25 mrad [107]. How strongly this affects the error on the rotation rate, varies with ω and the time resolution used in the experiment. To ensure that the encoder is ca-

pable of probing ω in the full range where we will measure, we perform test experiments at both constant T and constant Ω that cover the two relevant decades in ω. We compare the output of the encoder with the numbers that are found by the rheometer and see that they correspond well – see Fig 4.4.

When reading out the encoder at 1 kHz, we observe a significant 63 Hz signal caused by the shaking at this frequency. Filtering out this signal is not trivial, since it is distributed over a frequency band around 63 Hz with a width of the order of 1 Hz, as well as over the higher harmonics. We therefore decide to read out the encoder stroboscopically with a sample rate of 63 Hz, where we use the sync output of the function generator that is used to control the shaker as a trigger to read out θ (it triggers on the moment the sine goes through the equilibrium from negative to positive). This way, we always measure θ in the same position of the cycle, thereby suppressing the spurious signal caused by the shaker.

4.2.1 Protocol

Filling Height – As shown in Fig. 3.3, the value of Γ_c depends on the relative filling height $h \equiv H/r_s$. The reason for this Γ dependence stems from the details of the flow structure, as explained in Sec. 3.4.2. For low h, we have observed that Γ_c becomes close to 1, which makes the range of monotonic flow curves we can study inconveniently small. Therefore, we choose a relatively high filling height, $h = 0.6$, which, as we know from exploratory stress-controlled experiments, results in $\Gamma_c \approx 0.65$.

Control parameters – We perform two different types of measurements.

First, we measure flow curves $T(\Omega)$ in rate control to study the scaling of the shape of the flow curves around the critical point. To study the scaling of the flow curves, we measure a set of flow curves for $0.3 \leq \Gamma \leq 0.7$ with $\Delta\Gamma = 0.01$ and Ω =1.0, 0.63, 0.40, 0.25, 0.16, 0.1,..., 0.001 rps in 16 logarithmic steps. We average each point for 180 s, which is long enough to reach the steady state – see Sec. 3.2.

Second, we measure $\theta(t)$ in a stress-controlled experiment to probe the fluctuations in its derivative ω, for a range of torques and vibration amplitudes which form a grid in (T, Γ)-space. If we want data that is suitable to accurately determine the scaling of the fluctuations with Γ^*, we have to be certain that the grid is closely centered around the critical

point. From test measurements in stress control we know that $\Gamma_c \approx 0.65$ and $T_c \approx 30.5$ mNm. We have taken two data sets. In data set 1, we choose our 20x20 grid with T going from 28.9 mNm to 31.75 mNm in steps of $\Delta T = 0.15$ mNm and Γ going from 0.65 to 0.935 with $\Delta\Gamma = 0.015$. In data set 2, where we focus on what happens around the inflection points of the flow curves, we take Γ from 0.62 to 0.77 with $\Delta\Gamma = 0.01$, but different T values for each Γ around T_i. From exploratory measurements, we estimate that T_i [mNm] $\approx 34.64 - 5.16\Gamma$ and we choose the ten T-values such that they surround T_i with $\Delta T = 0.1$ mNm. In both data sets, we measure 40 min per (T, Γ) for good statistics and to be able to extract time scales up to a few minutes.

4.3 Theoretical Framework

By comparing the transition from slow to fast flow to the liquid-gas and the Ising ordered-disordered transitions, as shown in the mapping in Table 4.1, we obtain several predictions for the scaling behavior and values for the critical mean field exponents [108, 109].

Parameters – In this section we summarize the many parameters that we will use throughout this chapter. We denote the rotation rate by Ω if it concerns a control parameter or a time averaged value, and by ω if it is a time-dependent order parameter. When looking at scaling relations, we will quantify the flow rate with $l \equiv \log_{10}(\Omega/1 \text{ rps})$. Throughout this chapter we will see several examples that imply that l is the natural coordinate. For example, many properties of the system (for instance Eq. 4.2) scale with l via a power-law relation whereas the scaling in Ω would take a more complex form.

For each Γ, the flow curve has an inflection point (T_i, l_i). At the critical Γ_c, this is the critical point (T_c, l_c). We define the reduced $\Gamma^* \equiv (\Gamma - \Gamma_c)/\Gamma_c$ and $T^* \equiv (T - T_i)/T_i$, both of which are zero at the critical point (at the critical point, $T_i = T_c$ and $T^* \equiv (T - T_c)/T_c$).

Flow Curves – To examine the shape of the flow curves, we wish to determine their inflection points (T_i, l_i), as well as the slope at these inflection points $\chi^{-1} \equiv \partial T_i/\partial l_i$ and the distance between the local minimum and maximum, Δl, for $\Gamma^* < 0$. To obtain accurate values for T_i, l_i, χ^{-1} and Δl,

we do not wish to calculate numerical derivatives from our experimental data, but rather use simple polynomial fits. From the raw $T(l)$-curves that are shown in Fig. 4.5(a), we see that the shape of the flow curves around their inflection points is reminiscent of a third order polynomial, where the linear part dominates the inflection point and controls the slope around l_i. We therefore will fit the flow curves around the inflection point with:

$$T = a(l - l_i)^3 + \chi^{-1}(l - l_i) + T_i \, . \tag{4.2}$$

In the next section we will show that this fit is capable of fitting the flow curves in the region around the inflection point given by $-1.6 < l < 0$.

The susceptibility χ of a system describes its response to an applied field and diverges at the critical point. However, since we consider $T(l)$, the slopes at our inflection points vanish towards the critical point, which is why we denote this slope as χ^{-1}.

Based on what we can measure for our system, we can test the following three scaling relations:

$$T^* \sim l^{*\delta} \, , \tag{4.3}$$

$$\chi^{-1} \sim |\Gamma^*|^{\gamma} \, , \tag{4.4}$$

$$\Delta l \sim |\Gamma^*|^{\beta} \, . \tag{4.5}$$

The mean field values of these exponents are:

$$\delta = 3 \, , \tag{4.6}$$

$$\gamma = 1 \, , \tag{4.7}$$

$$\beta = 1/2 \, . \tag{4.8}$$

Note that we do not measure the value of δ, but based on the shape of the flow curves and mean field prediction, we have set it to $\delta = 3$. The fact that fit of the data to Eq. 4.2 works well justifies this assumption. As Δl is found by identifying the zero crossings of the derivative of $a(l-l_i)^3+\chi^{-1}(l-l_i)$, Δl and χ^{-1} are related. This results in the constraint $\gamma = 2\beta$. Hence, from the flow curves we can extract a single exponent (either γ or β); the determination of the other is then a consistency check.

Fluctuations – As diverging fluctuations are an important hallmark of critical behavior, we want to study the fluctuations in the velocity of the

flow. However, we measure the disk angle θ and we cannot a priori know that we are allowed to calculate a *velocity* for our fluctuating disk; for fluctuating systems such as a random walker, the velocity is not even defined.

Of course, because of the inertia of our driving disk, the velocity cannot grow arbitrarily large, and extremely rapid velocity fluctuations are suppressed. To get an idea of the relevant scales, we note that the moment of inertia of our disk and corotating grains $\approx 0.3\ \mathrm{g\,m^2}$. Even if we suddenly subject the disk to the typical driving torque of 30 mNm, we expect its rate to vary with 0.3 rps in 1/63 s. As the effective torque fluctuations are typically much smaller, we do not expect rate differences of the order of 0.1 rps between two consecutive data points. Therefore, we expect a smooth $\theta(t)$ that we *can* differentiate.

We will use two different methods to extract values for the magnitude σ^2 and characteristic time scale τ of $\omega(t)$.

First, we will show further evidence that we indeed probe $\theta(t)$ fast enough to evaluate its derivative ω, and then calculate its variance σ^2_ω as a measure for the magnitude of the fluctuations. The characteristic time scale τ_a is obtained from the autocorrelation function of l (which is $\log_{10}(\omega/1\ \mathrm{rps})$).

Second, we interpret the motion of our disk as the path of a massive random walker, whose behavior is given by an overall drift plus a noise η. To capture the effect of inertia, the noise η is not delta-correlated, but we assume it has an exponential correlation:

$$\langle \eta(t')\eta(t'')\rangle = \sigma_c^2 \exp(-|t''-t'|/\tau_c)\ , \tag{4.9}$$

where σ_c^2 is the magnitude and τ_c the time scale of the fluctuations. For a random walker with drift, the quantity to look at is $\sigma^2_{\Delta\theta}$ as a function of Δt. For a system with noise as in Eq. 4.9, this is given by [110]:

$$\sigma^2_{\Delta\theta} = 2\sigma_c^2\tau_c[\Delta t - \tau_c(1-e^{-\Delta t/\tau_c})]\ . \tag{4.10}$$

For small Δt, this reduces to $\sigma_c^2\Delta t^2$, *i.e.*, ballistic motion due to the correlated nature of η. In this regime, ω is well-defined. For large Δt, $\sigma^2_{\Delta\theta}$ approaches $2\sigma_c^2\tau_c\Delta t$, *i.e.* diffusive behavior (where $\sigma_c^2\tau_c$ is the diffusion constant D). We stress that, in this model, the complete behavior of $\sigma^2_{\Delta\theta}$ is governed by two parameters: σ_c^2 and τ_c.

In Sec. 4.5.6 we will show that the analyses via $\omega(t)$ and $\sigma^2_{\Delta\theta}$ produce similar results for σ^2 and τ; both the fluctuation magnitudes and correlation times are consistent between both methods.

The scaling relations we will test for the fluctuations are:

$$\sigma^2 \sim \Gamma^{*-\gamma} , \tag{4.11}$$

$$\tau \sim \Gamma^{*-\nu} . \tag{4.12}$$

The mean field values of these exponents are:

$$\gamma = 1 , \tag{4.13}$$

$$\nu = 1/2 , \tag{4.14}$$

where γ is the same as in Eq. 4.4. Of course, we measure the fluctuations as a function of both Γ^* and T^*, so if we want to look at the scaling only as a function of Γ^*, we have to decide for which T to select τ and σ^2. Since the critical point is the inflection of the curve for $\Gamma^* = 0$, we will take τ and σ^2 at the inflection point for each Γ^*.

In conclusion, we can determine *two* independent scaling exponents of our data; ν, which characterizes the divergence of the characteristic time scale; and $\gamma = 2\beta$, which can be obtained from the magnitude of the fluctuations, and from the steady state flow curves.

4.4 Flow Curves

In this section we will fit the flow curves with a cubic polynomial and demonstrate that the fit accurately describes the data. We will use the fit parameters thus obtained to determine Γ_c and to discuss how the flow curves vary with Γ. We then extract values for the inverse slope at the inflection point, χ, and the distance between the local minimum and maximum of the flow curve, Δl, and finally determine their scaling with Γ^*.

Fit – To determine the shape of the flow curves $T(l)$, we fit the flow curves with a cubic polynomial (Eq. 4.2):

$$T = a(l - l_i)^3 + \chi^{-1}(l - l_i) + T_i .$$

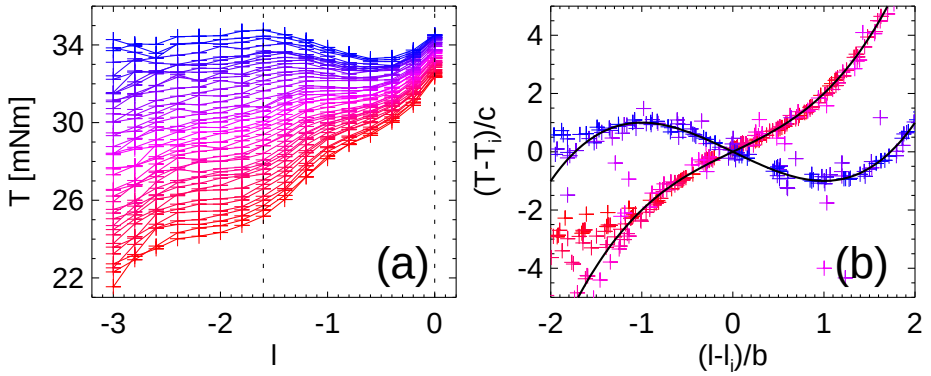

FIGURE 4.5: (a) The flow curves measured in rate control. The color indicates Γ from 0.3 (blue) to 0.7 (red). The dotted lines indicate the region of the curves we fit. (b) Using the fit to Eq. 4.2, we collapse the flow curves onto the master curves (plotted in black) $T - T_i = l_i + 1/2(l - l_i)^3 \pm 3/2(l - l_i)$, using the horizontal scale factor $b = \sqrt{|\chi^{-1}/3a|}$ and the vertical scale factor $c = \sqrt{|4(\chi^{-1})^3/27a|}$. Note that for Γ^* very close to 0, b and c become very small, which magnifies the small deviation between the fit and the data (see purple outliers for $\Gamma \approx 0.46$).

From the raw data, shown in Fig. 4.5(a), it can be seen that it is not possible to fit the flow curve over the full range of l with a cubic polynomial in l, as Eq. 4.2 is symmetric around (l_i, T_i), whereas the data is not. We find that the fit corresponds well to the data for all Γ if we limit the fitting range to $-1.6 < l < 0$ (we have verified that there is no strong dependence of the fit parameters on the choice of these boundaries).

To demonstrate that the fit accurately describes the data in this range, we collapse the flow curves using the fit parameters. To achieve a collapse, we plot $(l - l_i)/b$ on the horizontal axis and $(T - T_i)/c$ on the vertical axis. This way, the inflection point is shifted to the origin, and b and c are chosen such that the local maximum for $\Gamma^* < 0$ rescales to (-1,1). The actual values $b = \sqrt{|\chi^{-1}/3a|}$ and $c = \sqrt{|4(\chi^{-1})^3/27a|}$ are found by solving a simple quadratic equation derived from Eq. 4.2. We show that the rescaled data nicely collapses onto two branches in Fig. 4.5(b). The master curves, $T - T_i = l_i + 1/2(l - l_i)^3 \pm 3/2(l - l_i)$ are added in black.

The dependence of the four fit parameters of Eq. 4.2 on Γ is shown in Fig. 4.6. In (a), we plot χ^{-1}, which sets the slope at the inflection point, as function of the actual Γ. The curve is close to linear and its zero crossing

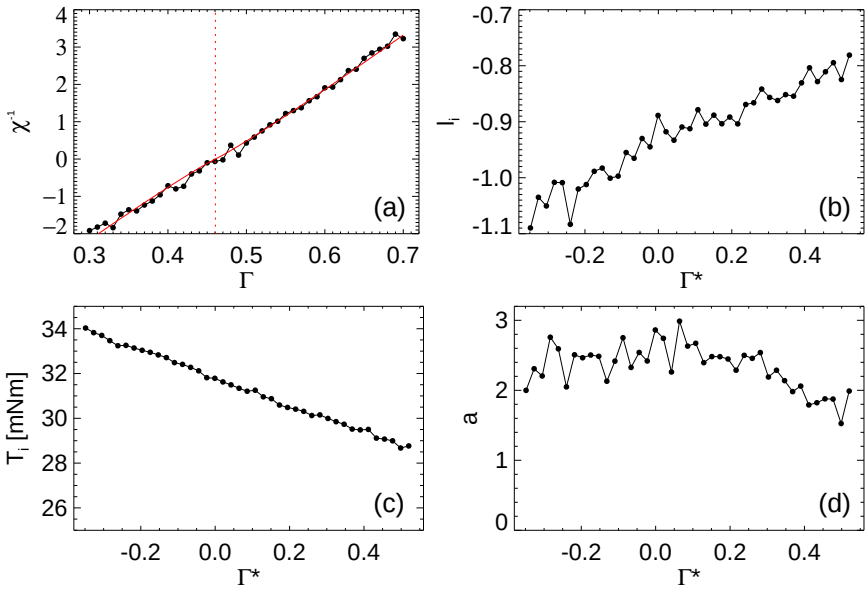

FIGURE 4.6: The four parameters of the fit with Eq. 4.2 as a function of Γ. χ^{-1} (a) is linear in Γ and crosses $\chi^{-1} = 0$ at Γ_c. We determine Γ_c and γ by fitting this data (the fit is overplotted in red); the dashed line indicates Γ_c *i.e.* $\Gamma^* = 0$. l_i (b) and T_i (c) vary linearly with Γ^*. a (plotted in (d)) is constant, especially around $\Gamma^* = 0$.

defines Γ_c. We use this data to determine Γ_c as well as the exponent γ (which is the scaling exponent of the slope at the inflection point as a function of Γ^*) by fitting the data with: $\chi^{-1} = \alpha \cdot \mathrm{sgn}(\Gamma - \Gamma_c)|\Gamma - \Gamma_c|^{\gamma}$. Doing so, we find $\gamma = 1.07 \pm 0.27$, and $\Gamma_c = 0.460 \pm 0.012$. The red dashed line in Fig. 4.6(a) represents Γ_c, *i.e.*, $\Gamma^* = 0$.

The rotation rate at the inflection point, l_i, increases linearly with Γ^* (Fig. 4.6(b)). The corresponding T_i, that decreases linearly with Γ^*, is plotted in Fig. 4.6(c). These scalings offer insight into the underlying mechanisms of the transition from slow to fast flow, and will be discussed in App. 4.A.3. The global cubic shape of the flow curve is set by the fit parameter a. In Fig. 4.6(d) we plot $a(\Gamma^*)$, which, especially around $\Gamma^* = 0$, is essentially constant. This agrees with the observation that, away from the inflection point, the flow curves exhibit a very similar shape (Fig. 4.5(a)).

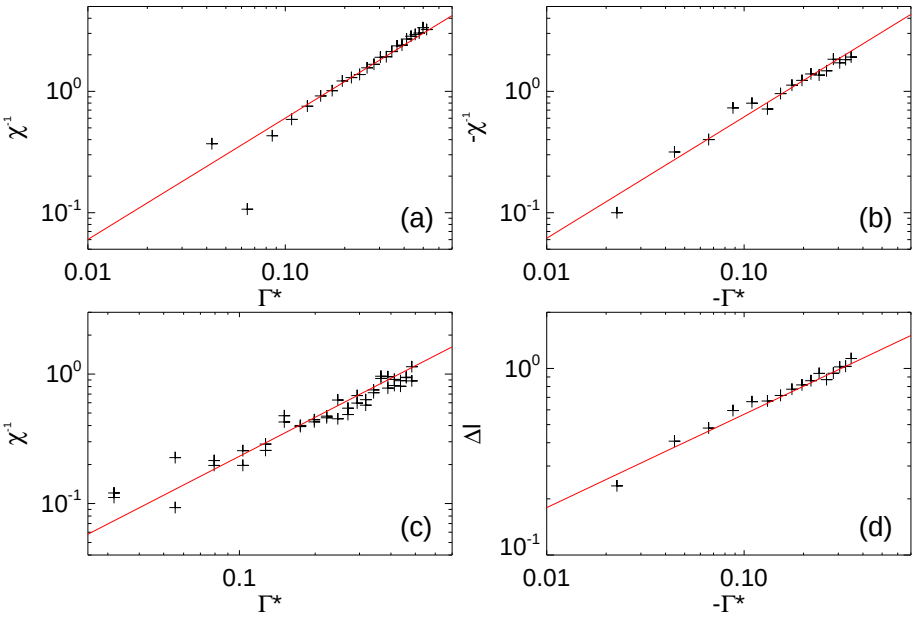

FIGURE 4.7: The scaling of χ^{-1} and Δl with Γ^*. (a) Susceptibility for rate control $\Gamma^* > 0$, (b) for $\Gamma^* < 0$, (c) for stress control. In (a-c), the red lines are linear fits. (d) Δl for rate control. Here, the red line is a square root fit.

Susceptibility χ – The susceptibility χ is defined as the inverse slope of $T(l)$ at the inflection point, and is expected to diverge as $\Gamma^* \to 0$. In Fig. 4.7(a), we plot χ^{-1} (actual slope; inverse susceptibility) versus Γ^* for $\Gamma^* > 0$, and in Fig. 4.7(b) we plot χ^{-1} for $\Gamma^* < 0$, both measured in *rate* control. In both cases, the scaling is close to linear as can be seen from the linear fits added in red. The prefactors for (a), 6.02±0.21 and (b), 6.16±0.25, are equal within error bars. In Fig. 4.6(a), we found an exponent $\gamma = 1.07 \pm 0.27$ for the full range in Γ^*. Here, we show that an exponent 1 (which is the mean field value) also matches the data well. The very nice linear relation between Γ^* and χ^{-1} indicates that our data agrees with a mean field description of the system.

We can also obtain χ^{-1} from the *stress*-controlled measurements that we use to study the fluctuations. The 400 measurements from data set 1 are performed as 40 torque ramps at constant Γ^*. From these 40 ramps,

we can extract 40 flow curves and extract χ^{-1}. The result is shown in Fig. 4.7(c) and tells us that also in stress-controlled experiments, χ^{-1} grows linearly with Γ^*. We note however that in this case, the prefactor is $2.32\pm$ 0.19, which is different than in Fig. 4.7(a-b). As we shall see in Sec. 4.5, the flow curves measured in T control are not exactly the same as the curves measured in Ω control. One possible explanation is that constant T and constant Ω measurements sample different ensembles, and $\langle\omega(T)\rangle$ and $\Omega(\langle T\rangle)$ need not coincide.

Rate Difference Δl **–** In Fig. 4.7(d), we plot Δl - which is extracted from the fit to the flow curve via $\Delta l = \sqrt{-4\chi^{-1}/3a}$ - as a function of Γ^*. In red, we add a fit with a power-law with exponent 1/2 (the mean value for β). We find that this fit accurately matches the data. As explained above, we have the constraint $\gamma = 2\beta$. The fact that this is indeed true for the data, supports our claim that the steady state flow curves can be described using a mean field picture.

Conclusion – In this section we have seen that that the mean field description works well to describe the shape of the flow curves. The scaling of χ^{-1} and Δl agrees with mean field scaling exponents $\gamma = 1$ and $\beta = 1/2$.

4.5 Fluctuations

In this section we will discuss the magnitude and time scale of the fluctuations in the $\omega(t)$ signals, which are measured in experiments at fixed Γ and T.

As explained in Sec. 4.3, the fluctuations will be analyzed using two different methods. In Sec. 4.5.2- 4.5.3, we will show that we measure $\theta(t)$ at high enough temporal resolution so that we can evaluate its derivative $\omega(t)$. Using $\omega(t)$, we then calculate the fluctuation magnitude σ^2_ω and time scale τ_a from the autocorrelation function of $l(t)$. In Sec. 4.5.4, we approach the problem from a statistical point of view by studying the evolution of $\sigma^2_{\Delta\theta}$ as function of time. Using Eq. 4.10, we obtain magnitude σ^2_c and time scale τ_c. In Sec. 4.5.5 we discuss how to locate the critical point in stress-controlled experiments, and in Sec. 4.5.6 we show the scaling of σ^2_ω and τ_a with Γ^*.

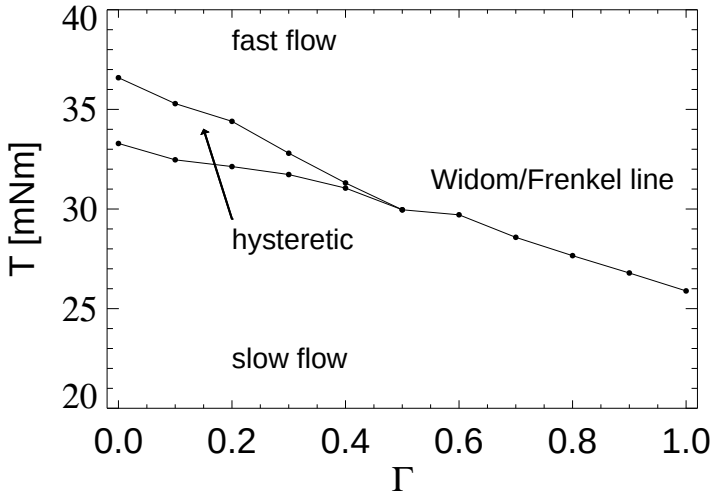

FIGURE 4.8: The slow and fast flow regime, separated by a hysteretic regime ($\Gamma^*<0$) and the Widom/Frenkel line ($\Gamma^*>0$) [111], in (T, Γ)-space.

4.5.1 Phenomenology

Before we study the velocity signals in detail, we identify the different regimes in (T, Γ)-space in Fig. 4.8. For $\Gamma < \Gamma_c$, we plot the values of T at the local minima and maxima of the flow curves. In between these two boundaries, the system is hysteretic. This means that if we do experiments in torque control in this regime, the flow is bistable and fluctuations may cause ω to be jumping back and forth between the slow and fast flowing branch. At Γ_c, these boundaries come together. For $\Gamma > \Gamma_c$, we plot a line which connects the torque values at the inflection point. This line - which is called Widom or Frenkel line [111] - signifies the smooth crossover between the slow and the fast flow, and it is here where we expect the fluctuations to peak for each Γ. While studying the behavior close to the Widom line, we will also identify several fundamental differences between the slow and the fast flowing regime. This suggests that the transition that we study is between two *flowing*, but very different, states.

A natural question to ask is what happens when the fluctuation experiments are performed in rate control. You could expect very large fluctuations in T for flow in the negative slope regime, since there is no con-

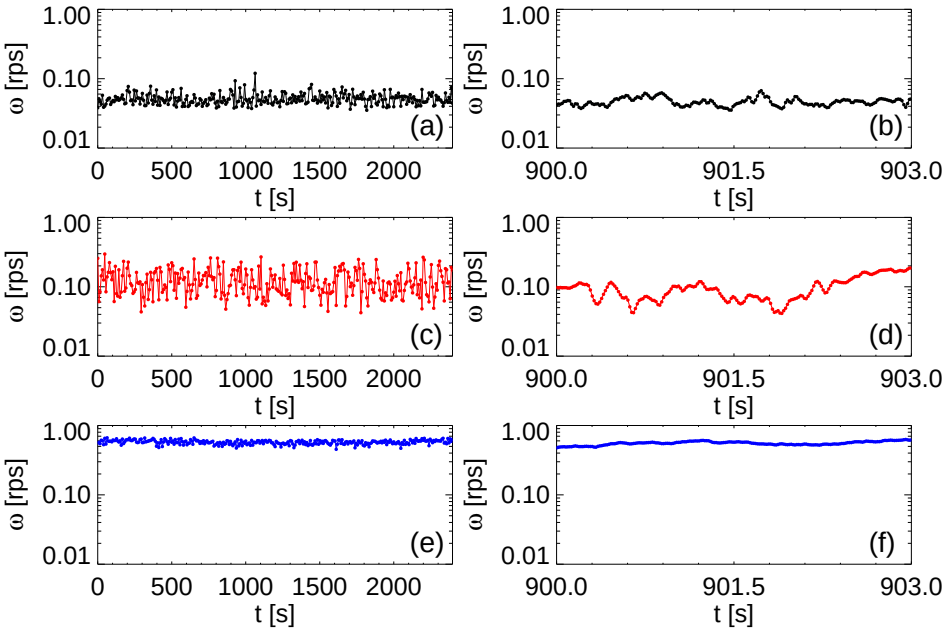

FIGURE 4.9: $\omega(t)$ for Γ just above Γ_c and $T < T_i$ (a-b), $T \approx T_i$ (c-d), $T > T_i$ (e-f). The vertical scale is equal for all panels to visualize that the fluctuations are the largest for $T \approx T_i$; b,d,f zoom in on shorter time scales. The fluctuations are much smaller for fast flow than for slow flow, but are maximal at the inflection point (Widom line).

stant T for which there is stable flow in this regime. Around the critical point the fluctuations could be small, since a small change in T results in a significantly different Ω. However, we found that these experiments cannot be performed in our setup. The problem is that the native mode of the rheometer is stress control, and rate-controlled experiments require a feedback system. The characteristic time of the feedback loop, the so-called csr-value, completely dominates the size of the fluctuations, and there is no clear relation between the amplitude of the fluctuations and the distance to the critical point.

4.5.2 Determination of the Velocity

In this section we study the raw signal, $\theta(t)$, and its derivative $\omega(t)$, to demonstrate that we probe $\theta(t)$ at a high enough temporal resolution to be

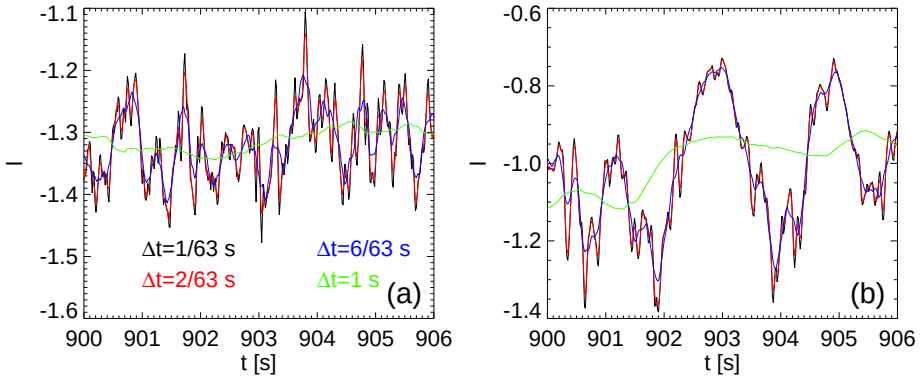

FIGURE 4.10: $\omega(t)$ calculated for four different values of Δt as indicated in the legend. (a) $\omega(t)$ for ($\Gamma^* = 0.060$, $T^* = -0.032$) (b) $\omega(t)$ for ($\Gamma^* = 0.060$, $T^* = 0.0032$). For $\Delta t = 1/63$ s, $2/63$ s and $6/63$ s, the signal looks roughly the same, only the fluctuations become smaller for longer averaging. For $\Delta t = 1$ s, which is longer than the τ corresponding to (a), the dominated features of the curve completely disappeared, in (b) $\tau \approx 1$ s, and the slow fluctuations are still present in the green signal.

allowed to take a derivative. In Fig. 4.9 we plot $\omega(t)$ (a three-point derivative of $\theta(t)$ with $\Delta t = 1/63$ s) for slow, intermediate and fast flow. Again it can be seen that the fluctuations are largest at intermediate flow rate. In panels (c,d,f) we show a magnification of the data which clearly shows the individual data points (in (a,c,e) we only plot each 500th point). On this scale, the signal appears smooth which means that θ does not correspond to purely delta-correlated diffusive behavior; rather, θ is sufficiently smooth on short time scales so that $\omega(t)$ is well-defined.

As an additional check to see if we extract a proper velocity, we calculate the three-point derivative of $\theta(t)$ for different Δt and show the results in Fig. 4.10. For $\Delta t = 1/63$ s, $2/63$ s and $6/63$ s, the signal looks quite similar. For $\Delta t = 1$ s (which we will show to be longer than the correlation time τ that corresponds to (a)), the dominant fluctuations are strongly suppressed. On the contrary, for the data in (b), for which we will show that $\tau \approx 1$ s, the dominant slow features of the curve are still visible in the curve for $\Delta t = 1$ s.

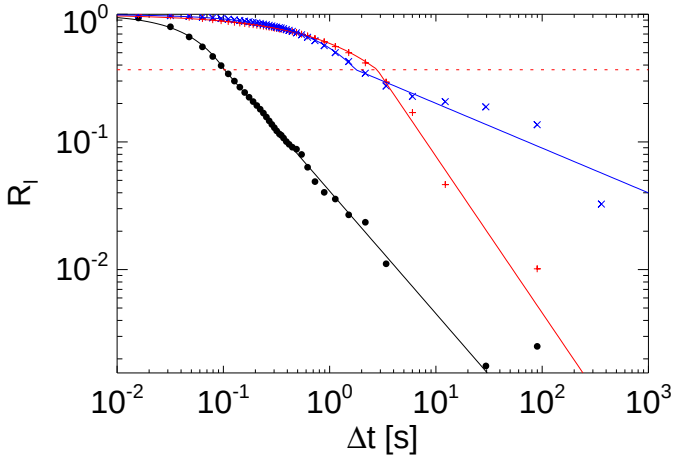

FIGURE 4.11: Autocorrelation functions R_l for the data in Fig. 4.9. For small Δt, the curves can be fitted with a stretched exponential. The black (•) curve is for slow flow and has a short time scale, the red (+) curve corresponds to large fluctuations and has the longest time scale. The blue (×) curve is for fast flow and also has a high τ. For large Δt, the curves take the shape of a power-law where the fast flow has the highest exponent.

4.5.3 Autocorrelation

Now that we have established that we have a well-defined $l(t)$, we will extract the characteristic time τ_a from its autocorrelation function $R_l(\Delta t)$. In principle, it would also be possible to directly calculate the autocorrelation function of $\theta(t)$. The reason that we do not do this, is that long time fluctuations in the signal will dominate the autocorrelation function and result in an ∞ time scale. If we first differentiate to get $l(t)$, we can see both the fast time scale (in the initial exponential decay) and the longer time scale (in the tail of the correlation function). The autocorrelation function is defined as:

$$R_l(\Delta t) = \frac{\sum_{k=0}^{N-\Delta t-1}(l_k - \bar{l})(l_{k+\Delta t} - \bar{l})}{\sum_{k=0}^{N-1}(l_k - \bar{l})^2}, \tag{4.15}$$

where N is the number of data points in $l(t)$ after the removal of a transient. We removed a 4 min transient from each data set, which even for

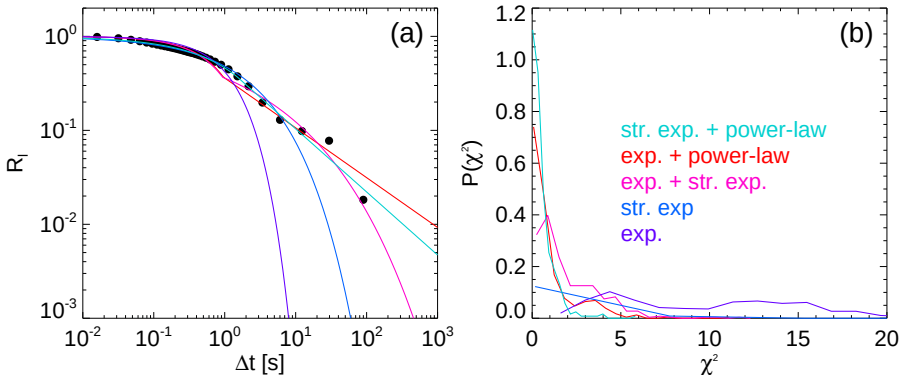

FIGURE 4.12: (a) The autocorrelation function R_l for ($\Gamma^* = 0.19$, $T^* = -0.024$) fitted with the five different fit functions that are indicated in (b). (b) The distributions χ^2 for the five fits. Clearly, the fit with Eq. 4.16 is the best.

the slowest runs corresponds to a strain of 7 rotations – enough to be sure that the system has reached a steady state.

In Fig. 4.11 we show $R_l(\Delta t)$ for the slow, intermediate, and fast flow curves shown in Fig. 4.9. The curves have significantly different and complex shapes and cannot easily be collapsed or fitted with a standard exponential decay fitting function. In this section we will carefully investigate in what way best to extract a time scale from these correlation functions.

We will start by finding a fitting function for R_l. The data in Fig. 4.11 suggests that the autocorrelations are stretched exponentials for small Δt, crossing over to power-laws for larger Δt. This is illustrated in Fig. 4.12. In (a), we show fits to R_l for a slow flow run ($\Gamma^* = 0.060$, $T^* = -0.0032$). Attempts to fit the data with an exponentially decaying function (purple) and stretched exponential (blue) fail for large Δt, where R_l decreases more slowly. We will therefore use a fit that is a linear combination of two functional forms, one for $\Delta t < \tau_a$ and another for $\Delta t > \tau_a$. We start with a three-parameter fit that combines stretched exponential decay and a power-law (in cyan):

$$R(\Delta t) = \frac{s(\tau_a)}{e}(\Delta t/\tau_a)^{\eta} + [1 - s(\tau_a)]e^{-(\Delta t/\tau_a)^{\zeta}} , \tag{4.16}$$

where ζ is the stretching exponent, and η is the slope of the power-law for large Δt. $s(\tau_a)$ is a logistic function that governs the crossover from stretched exponential to power-law, with its center around τ_a:

$$s(\tau_a) = \frac{1}{1 + e^{\lambda(\log_{10}(\tau_a/\Delta t))}} , \tag{4.17}$$

where $s \approx 0$ for $\Delta t < \tau_a$, $s \approx 1$ for $\Delta t > \tau_a$, and λ determines the width of the crossover. We find that the crossover in our data is sharp and verify that the fit does not significantly depend on λ as long as $\lambda \gtrsim 50$ (we pick $\lambda = 100$).

In Fig. 4.12(a), we compare this three-parameter fit with a two-parameter combination of a simple exponential decay and a power-law (Eq. 4.16 with $\zeta = 1$, plotted in red):

$$R(\Delta t) = \frac{s(\tau_a)}{e}(\Delta t/\tau_a)^{\eta} + [1 - s(\tau_a)]e^{-\Delta t/\tau_a} , \tag{4.18}$$

and a two-parameter combination of a simple and a stretched exponential (pink):

$$R(\Delta t) = s(\tau_a) \times e^{-(\Delta t/\tau_a)^{\zeta}} + [1 - s(\tau_a)]e^{-\Delta t/\tau_a} . \tag{4.19}$$

In Fig. 4.12(a) we see that only the fit with Eq. 4.16 is capable of grasping all the features of the data. We verify if this is the case for all the runs by plotting the distributions of the quality of the fits, χ^2, for the five different functional forms that are shown in Fig. 4.12(a) in Fig. 4.12(b). The high peak at low χ^2 in the cyan curve shows that the fit with Eq. 4.18 is clearly superior. This is not surprising as it is the one with the most fit parameters. However, Fig. 4.12 shows that the three-parameter fit is *significantly* better than the two-parameter fits, suggesting that we need three fit parameters to describe the complex shape of R_l.

To see how R_l varies throughout our parameter space, we plot the values of τ_a, ζ and η as a function of Ω and Γ in Fig. 4.13. Even though T is the control parameter, we plot as a function of Ω so that we can compare τ_a to the duration of one revolution $1/\Omega$.

In Fig. 4.13(a), we see that, for each Γ, τ_a initially increases with Ω and reaches a peak for $\Omega \approx 0.2$ rps. For large Ω, τ_a decreases but does not drop back very much, and approaches Ω^{-1} for large Ω – this suggests that in this regime, correlations due to the periodicity of the system start

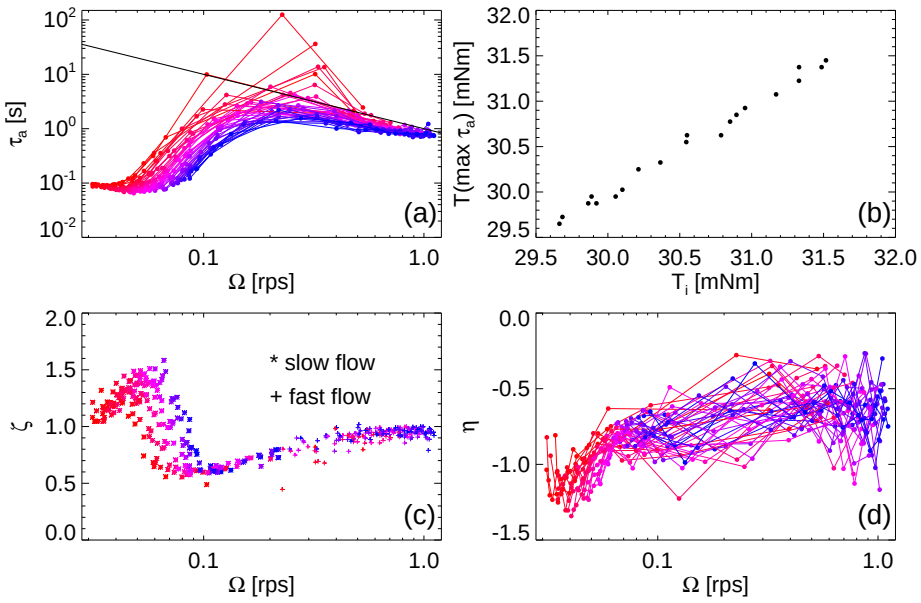

FIGURE 4.13: The fit parameters of the autocorrelation function. (a) the time scale τ_a as a function of Ω, color coded by Γ (red corresponds to low Γ). The black line indicates $\tau_a = 1/\Omega$. (b) The T for which the time scale is longest $T(\max \tau_a)$ is the torque at the inflection point T_i. T_i is found using a fit with Eq. 4.2. (c) The stretching exponent ζ. The (*) and (+) symbols reflect slow and fast flow. (d) The power-law slope η of the autocorrelation for long Δt.

to dominate. Nevertheless, the data shows a clear peak, which is largest for $\Gamma^* \approx 0$.

The dependence of ζ (Fig. 4.13(c)) is more complex. For slow and fast flow, $\zeta \approx 1$, whereas in the intermediate range, ζ varies between 1.5 and 0.5. Surprisingly, the region where ζ varies most dramatically, $\Omega \approx 0.07$ rps, is significantly below Ω_i (as indicated by the plot symbols).

The dependence of η (Fig. 4.13(d)) is noisy but there is a trend that η is lower for slow flow. In Fig. 4.13(b) we plot the T at which the time scale peaks versus the inflection torque T_i and see that, as expected, the time scale peaks at the inflection point.

We will now investigate the behavior of τ_a for large Ω, where $\tau_a \approx \Omega^{-1}$. In Fig. 4.14, we test if a concomitant periodicity is visible in the raw data

for a fast flow run. In (a), we plot ω as a function of θ but find that it is hard to see which frequencies are present in the signal. Therefore, we plot the power spectrum (PS) as a function of frequency of $\omega(\theta)$ in θ space (f_r) in (b). We see that $PS \sim f_r^{-2}$, which corresponds to normal Brownian noise. Nevertheless, zooming in on the spectrum around $f_r = 1$, we find that there is a 1 rev periodicity in the data (inset).

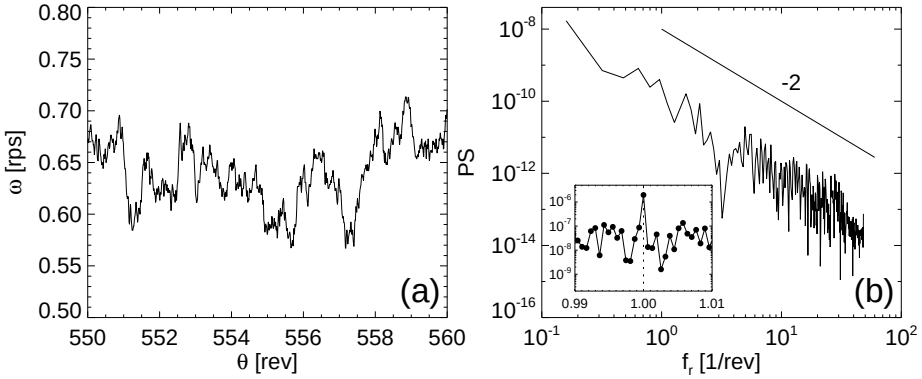

FIGURE 4.14: (a) ω as a function of θ. For this run, $\tau_a = 1.24$ s whereas $\Omega^{-1} = 1.53$ s. (b) The power spectrum (PS) of $\omega(\theta)$ scales as $PS \sim f_r^{-2}$, which corresponds to normal Brownian noise. In the inset, we show the spectrum around $f_r = 1$, which shows that there is a 1 rev periodicity in the system.

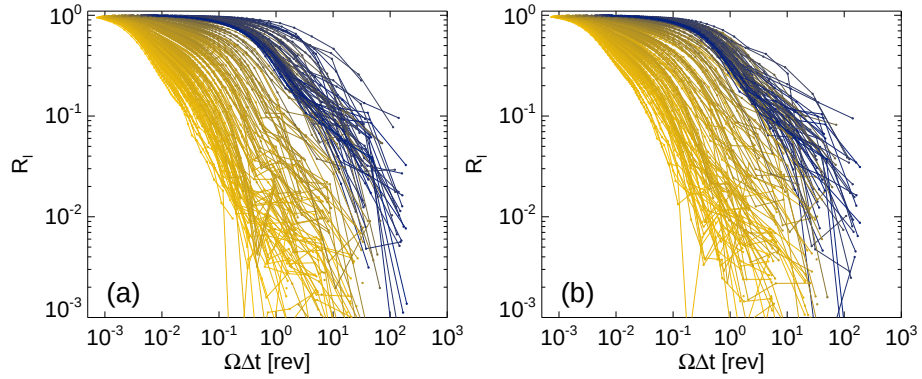

FIGURE 4.15: All the autocorrelation functions R_l for data set 2. In (a), we show the uncorrected data. In (b), we show R_l where the 1 rev component in filtered out before calculating the correlation function. In both cases, there is a (blue) cluster of fast flowing curves with a $\tau_a \approx \Omega^{-1}$.

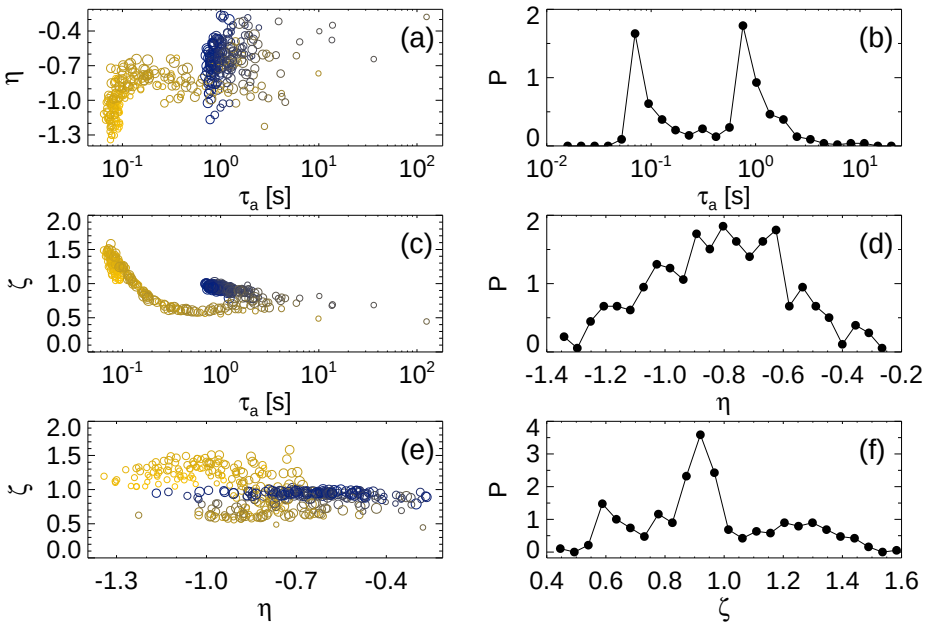

FIGURE 4.16: Scatter plots of τ_a vs η (a), τ_a vs ζ (c) and η vs ζ (e). The color of the data points indicates l (yellow: $l < l_i$, green: $l \approx l_i$, blue: $l > l_i$), the symbol size indicates Γ where a larger blob corresponds to a higher Γ. The local blobs show how R_l is systematically different for flow, intermediate and fast flows. These blobs are also visible in the distributions of τ_a (b), η (d) and ζ (f).

We want to investigate whether filtering out the Ω^{-1} component from $l(t)$ significantly changes the signal; this might make the results for slow and fast flow more comparable. In Fig. 4.15 we show all the correlation functions for data set 2 for both the unfiltered (a) and the filtered (b) case. We find that although the filtering affects R_l, in both panels of the figure there is a cluster of (blue) curves for fast flow with a time scale of approximately Ω^{-1}. This suggests that the behavior of $\tau_a \sim \Omega^{-1}$ is not only caused by a spurious Ω^{-1} component in the spectrum.

To further investigate qualitative differences between slow and fast flows, we study the results of the fit with Eq. 4.16 in more detail in Fig. 4.16. The scatter plots of τ_a vs η (a), τ_a vs ζ (c) and η vs ζ (e) show several blobs, which we believe to correspond to physically different flow regimes. In (a),

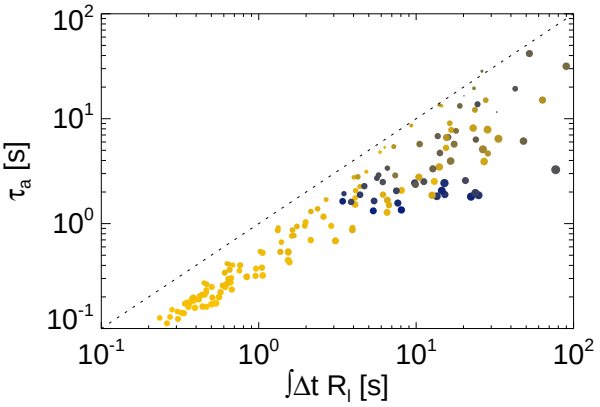

FIGURE 4.17: A scatter plot of τ_a vs $\int \Delta t R_l$ for data set 2 shows a good correspondence. The correlation is not perfect, which is caused by the complex shape of R_l. This can be seen from the size of symbols that represent η (larger symbols are larger η). A large η results in a large area under the curve and a relatively large $\int \Delta t R_l$.

there are two clear blobs, one at low τ_a for slow flow and one at high τ_a for fast flow. In (c), we see a systematic relation between τ_a and ζ, and a large blob arises for fast flow at $\zeta \approx 1$. Panel (e) shows that slow, intermediate, and fast flow are well separated with different ζ, whereas within one flow regime, there is a large spread in η. The different regimes arise as peaks in the distributions of τ_a (b) and ζ (f). The blobs in Fig. 4.16 suggest that the dominant fluctuations in the slow (quasi-static) and fast flow (inertial) regime might be caused by different physical phenomena.

Because of the three-parameter form of our fit, and the complex variation and dependencies of the fit parameters, doubt might arise on the values found for τ_a. We therefore extract a time scale from R_l without having to fit, by evaluating its integral over time. Due to long time fluctuations in R_l, the integral over R_l does not converge to zero but rather slowly fluctuates around zero, which makes the integral of R_l for $\Delta t \to \infty$ ill-defined. To get a well-defined value for $\int \Delta t R_l$, we stop integrating once $R_l \leq 10^{-2}$ – this leads to robust estimates for $\int \Delta t R_l$, not strongly dependent on the value of the cut-off.

In Fig. 4.17 we show a scatter plot of τ_a vs $\int \Delta t R_l$ which shows a good correspondence. Nevertheless, systematic deviations can be seen: for ex-

ample, large values of η (large symbols) lead to $\int \Delta t R_l > \tau_a$.

Conclusion – In this section we have shown that we can fit the autocorrelation function R_l with Eq. 4.16 and obtain τ_a. The fit parameters systemically vary with T and Γ. Not only do we see that τ_a increases towards the critical point, but we also find that the fits are systematically different for flow rates above and below the critical point, suggesting qualitative differences between fast and slow flows. The correspondence between τ_a and $\int \Delta t R_l$ indicates that we have extracted a robust time scale from $l(t)$.

4.5.4 Statistics of $\Delta\theta$

In this section we will analyze the data by looking at the statistics of $\Delta\theta$. This way, we avoid having to calculate the instantaneous velocity of the probe, but instead, look at the fluctuations in $\Delta\theta$ around the overall drift $\langle\theta\rangle = \Omega\Delta t$. By fitting $\sigma^2_{\Delta\theta}(\Delta t)$ to Eq. 4.10:

$$\sigma^2_{\Delta\theta} = 2\sigma_c^2\tau_c[\Delta t - \tau_c(1 - e^{-\Delta t/\tau_c})] \,,$$

we get values for the magnitude σ_c^2 and time scale τ_c of the fluctuations, independent of those obtained from l.

We calculate $\Delta\theta$ via $\Delta\theta = \theta(t + \Delta t) - \theta(t)$ for $\Delta t = \mathrm{ceil}(10^{n/5})/63$, with $n = 0, 1, .., 23$ (as before, we always remove a 4 min. transient).

In Fig. 4.18 we show distributions of $\Delta\theta$ for slow and fast flows and different Δt. It is clearly visible that the center of the distributions moves to larger $\Delta\theta$ for larger Δt, which is an indication that the fluctuations do not dominate the overall drift of the signal.

In Fig. 4.19 we show the rescaled distributions $(\Delta\theta - \langle\Delta\theta\rangle)/\sigma_{\Delta\theta}$, where $\sigma_{\Delta\theta} = \sqrt{\langle(\Delta\theta - \langle\Delta\theta\rangle)^2\rangle}$, for slow (a), intermediate (c), and fast (e) flows. We find that these rescaled pdf's for different Δt collapse reasonably well; hence their variation with Δt can be captured by $\sigma_{\Delta\theta}$. The pdf's typically are asymmetric and have the shape of skewed Gaussians. There is a trend that for slow flow, the pdf is positively skewed whereas for fast flow, it is negatively skewed. We suggest that this originates from the fact that the flow curve becomes flatter towards the inflection point. We expect that fluctuations in ω can be larger where the flow curve is flatter. This leads to an asymmetry in $P(\Delta\theta)$. Note that for fast flows, the inflection point is so far away that the pdf becomes symmetric and Gaussian – see *e.g.* Fig. 4.19(e).

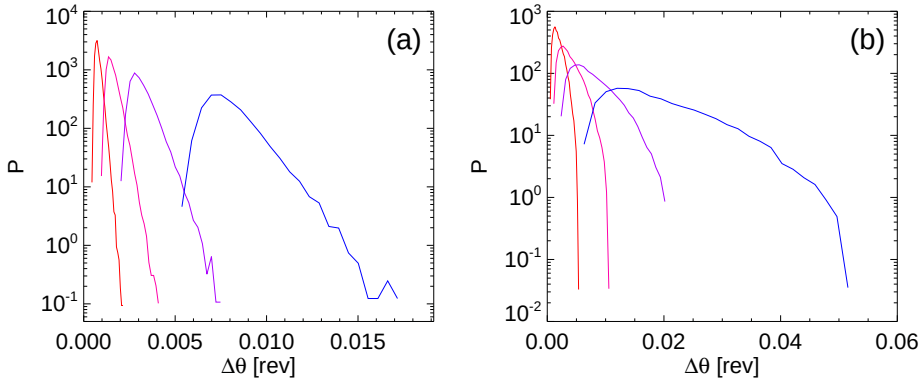

FIGURE 4.18: The distributions of $\Delta\theta$ for examples of slow flow (a) and fast flow (b) for $\Delta t = 1/63, 2/63, 4/63, 10/63$ s. The center of the distributions move to larger $\Delta\theta$ for larger Δt, which indicates that the fluctuations do not dominate the signal and that a clear average l can be extracted. The precise shape of the distributions depends on the distance to the critical point and will be discussed below.

We proceed our analysis by calculating the variance of $\Delta\theta$, $\sigma^2_{\Delta\theta}$ (equivalent to the mean squared displacement) as a function of Δt, and plot $\sigma^2_{\Delta\theta}/\Delta t$ as function of Δt in Fig. 4.19(b,d,f). For ballistic behavior, $\sigma^2_{\Delta\theta}/\Delta t$ grows linearly with Δt, whereas for a diffusive system, $\sigma^2_{\Delta\theta}/\Delta t$ is a constant (we divide by Δt because it is easier to identify a plateau than a line with slope 1). In Fig. 4.19, we see both kinds of behavior, and observe ballistic behavior for small Δt and a crossover to a plateau at long times. The fact that the crossover occurs for $\Delta t > 1/63$ s, agrees with our claim that we are allowed to differentiate $\Delta\theta$ on a time scale of $1/63$ s to obtain ω.

For most of our data we do not observe a nice plateau, but instead, see the curve bend up again for $\Delta t > 100$ s (see for example Fig. 4.19(b,f)). This, we believe, is caused by longer time scale fluctuations beyond the scope of this analysis. For even larger Δt, the curve drops because the magnitude of the fluctuations in l is limited and cannot grow indefinitely as it does for a diffusive system.

To obtain σ_c^2 and τ_c, we fit $\sigma^2_{\Delta\theta}$ with Eq. 4.10 and overplot the fit in red. As a result of the long time scale fluctuations and the finite measuring time, the fit is not always good for large Δt. However, as we shall see

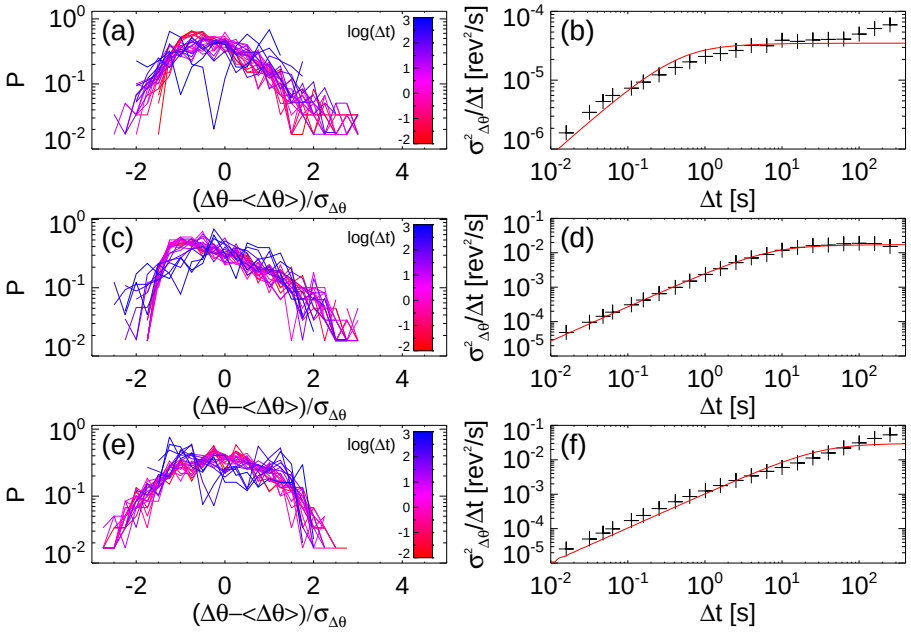

FIGURE 4.19: The rescaled distributions $(\Delta\theta - \langle\Delta\theta\rangle)/\sigma_{\Delta\theta}$ and $\sigma^2_{\Delta\theta}/\Delta t$ as function of Δt for slow flow ($\Gamma^* = 0.09$, $T^* = -0.033$ (a-b)), intermediate flow ($\Gamma^* = 0.09$, $T^* = -0.0044$ (c-d)) and fast flow ($\Gamma^* = 0.09$, $T^* = 0.15$ (e-f)). The data in (f) does initially start to flatten, but never reaches its plateau and then bends up again. The resulting shape cannot precisely be fitted with Eq. 4.10. However, reasonable values for σ_c^2 and τ_c can still be extracted.

in Sec. 4.5.6, the region where the fit is good, is large enough to extract proper values for σ_c^2 and τ_c.

4.5.5 Locating the Critical Point

Before we can proceed to the scaling of the time scale and magnitude of the fluctuations with Γ^*, we have to identify Γ_c. Finding the critical point is more difficult in stress-controlled than in rate-control experiments. In rate control, we simply plot χ^{-1} and determine the zero crossing, but in stress control, this is much harder to determine since we cannot measure the "negative slope" parts of the flow curves. In addition, we have very few data points around the inflection point, because a small increase in T

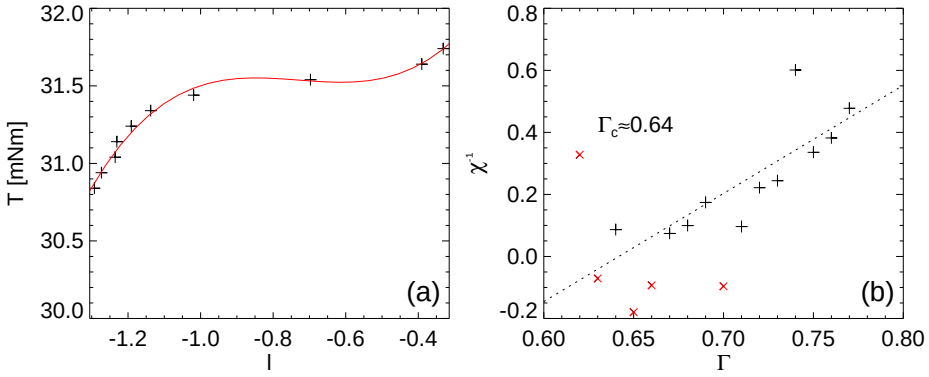

FIGURE 4.20: (a) The flow curve for $\Gamma = 0.65$ and a fit with Eq. 4.2. (b) The slope at the inflection point, χ^{-1}, as a function of Γ. We fit the data to obtain Γ_c and find Γ_c=0.64±0.03.

results in a large increase in Ω near the critical point – the grids of data points in torque or rate control are different.

In Fig. 4.20(a), we show the flow curve, measured in T-control, for $\Gamma = 0.65$. In red, we add a fit with Eq. 4.2 to obtain a value for χ^{-1}. We do this for all Γ, and plot all the values of χ^{-1} vs Γ in Fig. 4.20(b) (measuring flow curves in stress control will be discussed in more detail in App. 4.A.2). We want to compute where this relation crosses zero. For certain Γ, there is so little data around the inflection point that the fit yields an unrealistic (typically negative) value for χ^{-1}. We decide to not take these points into account and draw them in red ($\times$). Using the rest of the data (indicated by black (+)), we find $\Gamma_c = 0.64 \pm 0.03$.

As an alternative method, we can look at the fluctuation data to determine Γ_c. As explained in Sec. 4.5.1, the $\omega(t)$ signal is bistable in the hysteretic regime. This means that here, a pdf of $\omega(t)$ will be multi-humped. Γ_c is then the smallest value of Γ for which we do not observe this bistable behavior. In Fig. 4.21(a) we show the distributions for $\Gamma = 0.65$ and 10 increasing values of T. For low T, P is nearly Gaussian and as T increases, a new local maximum develops at large ω. Moreover, as T crosses through T_i, the center makes a big jump towards an ω that corresponds to fast flow. P now again takes a Gaussian shape.

To decide if a certain $P(\omega)$ is multi-humped, we want to identify its local maxima. We do this as follows: for slow flow, we find the maximum

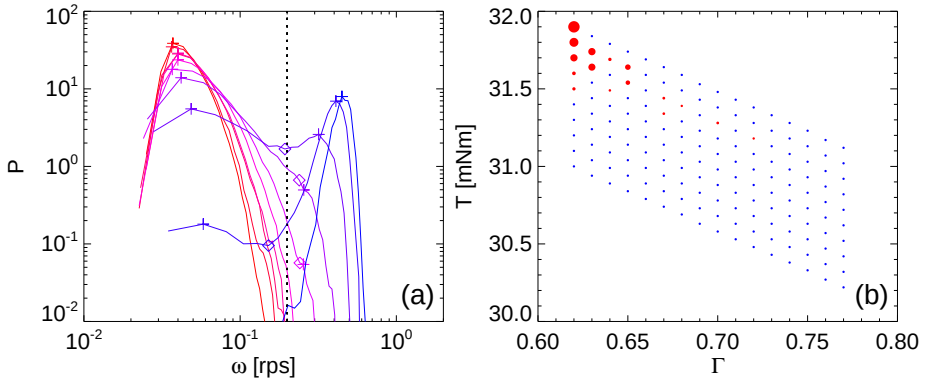

FIGURE 4.21: (a) Distributions $P(\omega)$ for $\Gamma = 0.65$ and varying T. P goes from monostable slow flow (red) via bistable (purple) to monostable fast slow (blue). The + and $\diamond$ symbols indicate the local minima and maxima of P. The black dashed line at 0.2 rps represents the separation between slow and fast flow. (b) Identification of the bistable (red) and monostable (blue) points in T, Γ-space. The size of the dot represents H (see Eq. 4.20).

of the curve (we call this s_+) for $\omega < 0.1$ rps, for fast flow, we take f_+ for $\omega > 0.25$ rps. For intermediate flow rate, we identify the minimum i_- for 0.1 rps$\leq \omega \leq 0.25$ rps. We now say $P(\omega)$ is bistable if $s_+ > i_-$ and $f_+ > i_-$, and both s_+ and $f_+ > 0.1$ (to eliminate hits where in a low, noisy tail, a local maximum, by accident, is larger than the center dip). To quantify the bistability of $P(\omega)$, we define:

$$H = \min\left(\frac{s_+}{i_-}, \frac{f_+}{i_-}\right) - 1\,; \tag{4.20}$$

for monostable curves, we define $H \equiv 0$. In Fig. 4.21(b) we show our data set 2 in (T, Γ)-space where a blue or a red point respectively indicates a monostable or bistable state. The size of the data point represents H. There is a clear blob of large red points for $\Gamma \leq 0.65$ which suggests $\Gamma_c \approx 0.65$. However, for larger Γ, there are still some bistable points, but the corresponding H is very low. This means that close to the Widom line, the fluctuations can be large for $\Gamma > \Gamma_c$, but the pdf is just broad and does not indicate significant bistable behavior.

The methods of Fig. 4.20 and Fig. 4.21 result in a similar value for Γ_c. The large fluctuations at the Widom line make it difficult to be very

precise, but we estimate $\Gamma_c = 0.65 \pm 0.01$ and $T_c = 31.6 \pm 0.1$ mNm. This value for Γ_c differs significantly (30%) from the one that was found for the rate-controlled measurements in Sec. 4.4. This is surprising and shows that, at least around Γ_c, rate and stress control experiments are not simply physically equivalent. We believe that the reason for this lies in the nature of the fluctuations, which are different in rate- (because of the feedback loop of the rheometer) and in stress-controlled experiments.

4.5.6 Scaling of Fluctuations

We want to study the scaling of the magnitude and time scale of the fluctuations with the distance to the critical point. Before we can do this, we need to carefully define which quantities we will consider exactly for the scaling.

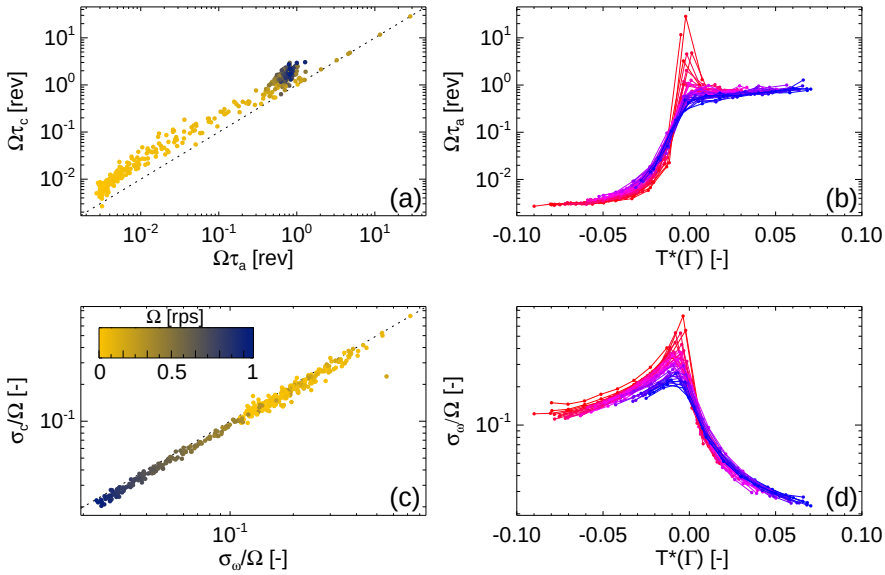

FIGURE 4.22: (a) The relation between $\tau_a\Omega$ (from the autocorrelation) and $\tau_c\Omega$ (from the crossover from ballistic to diffusive in $\sigma^2_{\Delta\theta}(\Delta t)$) is linear. (b) $\tau_a\Omega$ as function of T^*, color coded by Γ, where red indicates a Γ close to Γ_c. (c) The good correspondence between σ_ω/Ω and σ_c/Ω. (d) σ_ω/Ω as function of T^*.

We have determined two different *time scales*: τ_a, from the autocorrelation function, and τ_c from the crossover from ballistic to diffusive in $\sigma^2_{\Delta\theta}(\Delta t)$. Of course, there is another time scale in our system, which is Ω. To correct our time scales for this overall time scale Ω, we will consider the scaling of the characteristic strain $\tau_a\Omega$. In Fig. 4.22(a), we show a scatterplot of $\tau_a\Omega$ vs $\tau_c\Omega$. It shows that there is a great proportionality between τ_a and τ_c, and hence the two different methods we used to extract a time scale from the data.

In Fig. 4.22(b) we show $\tau_a\Omega$ as a function of Γ^* and T^*. We find that these curves have similar shape and there is a systematic trend that $\tau_c\Omega$ increases when approaching the critical point either in the Γ or in the T direction. This is similar to critical phenomena, for which the time scale diverges towards the critical point.

To characterize the *magnitude* of the fluctuations we also have two options. First, we take the derivative of $\theta(t)$, $\omega(t)$, and take its variance σ^2_ω as a measure for the fluctuations. Alternatively, from fitting $\sigma^2_{\Delta\theta}(\Delta t)$ with Eq. 4.10, we get a fluctuation magnitude σ^2_c. To get a dimensionless magnitude, we will consider σ_ω/Ω. In Fig. 4.22(c) we plot σ_c/Ω vs σ_ω/Ω and see a nearly perfect correspondence. This means that we are confident that we have extracted a proper magnitude of the fluctuations. In (d), we show σ_ω/Ω as a function of T^* and Γ^*. In this case, very clearly, σ_ω/Ω increases towards the critical point both in the T and Γ^* direction. Since the data peaks at $T^* = 0$ for all Γ, this data is very suitable to determine the scaling of σ_ω/Ω with Γ^*.

To test the scaling relations (Eq. 4.11, 4.12), we want to investigate how $\tau_a\Omega$ and σ_ω/Ω scale with Γ^*. As explained in Sec. 4.3, we take the values of $\tau_a\Omega$ and σ_ω/Ω at the inflection point for each Γ. There is however the complication that in T-controlled experiments, we do not have much data close to the inflection point – see Fig. 4.20(a). To account for this problem, we want to estimate what the value of σ_ω/Ω would be precisely at T_i. We do this by finding the maximum of $\sigma_\omega/\Omega(T)$ by performing a fit. We find that the best way to find the maximum is by plotting $\sigma_\omega/\Omega(l)$. In this representation, we find that we can fit the data for all Γ using a Gaussian as functional form:

$$\sigma_\omega/\Omega = a + b \cdot \exp\left(\frac{-(l-l_i)^2}{d}\right) . \tag{4.21}$$

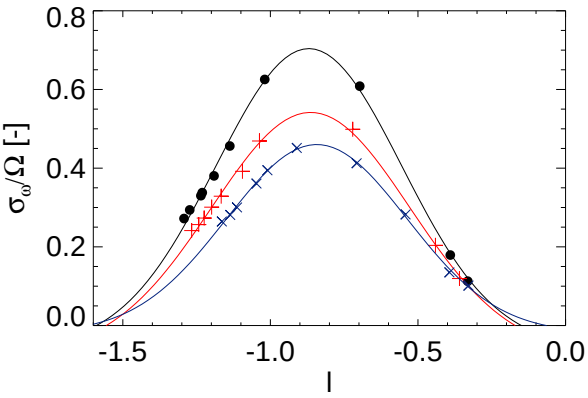

FIGURE 4.23: To estimate the value of σ_ω/Ω exactly at the inflection point, we fit $\sigma_\omega/\Omega(l)$ with Eq. 4.21. The three examples presented here are for $\Gamma^* = 0.019$ (black •), 0.097 (red +) and 0.18 (blue ×).

In Fig. 4.23 we show that this works well for $\Gamma^* = 0.019$, 0.097 and 0.18. The value of the maximum is then simply extracted from the fit as $a + b$. We note that we found this fit function empirically and have no reason to believe that Eq. 4.21 is an actual scaling function.

In Fig. 4.24 we show the peak values of $\tau_a\Omega$ (a) and σ_ω/Ω (b) at the inflection point as a function of Γ^*. We combine the data of data set 1 (black) and data set 2 (yellow) to cover a larger range in Γ^*. We see that both $\tau_a\Omega$ and σ_ω/Ω depend on Γ^* via a power-law, and want to extract the corresponding critical exponents. Note that, as we now look at the standard deviation σ_ω rather than the variance, we also have to take the square root of Eq. 4.11, which means we now obtain a value for the critical exponent $\gamma/2$.

The values of the exponents strongly depend on the value of Γ_c. Because of the error bar on Γ_c, we decide to neglect the data with $\Gamma^* < 0.05$ (indicated by the dotted line in Fig. 4.24). We fit the data with a power-law (plotted in red) and find $\nu = 0.94 \pm 0.47$ (mean field: $\nu = 1/2$) and $\gamma/2 = 0.47 \pm 0.22$ (mean field: $\gamma/2 = 1/2$).

For γ, our data is consistent with the mean field value $\gamma = 1$, both for the slope at the inflection point of the flow curve and the magnitude of the

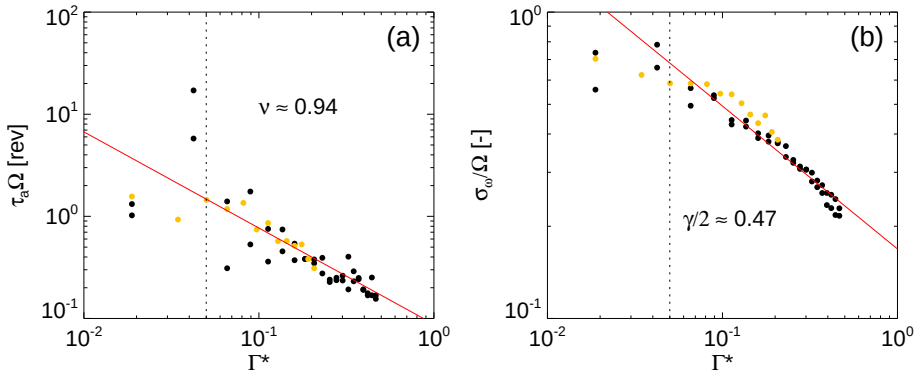

FIGURE 4.24: $\tau_a\Omega$ (a) and σ_ω/Ω (b) as found using the fit with Eq. 4.21 as a function of Γ^*. The black data is for data set 1, the yellow data for data set 2. We fit the data with a power-law (plotted in red) and find $\nu = 0.94 \pm 0.47$ and $\gamma/2 = 0.47 \pm 0.22$.

fluctuations. This supports our picture (Eq. 4.1) that the fluctuations for certain T and Γ are closely related to the local slope of the flow curve. If the $T(\Omega)$ flow curve is flatter, the corresponding fluctuations are larger.

The exponent ν, corresponding to the time scale, deviates from the mean field value (even though the mean field value of $1/2$ is just within the error bar). We interpret this as an indication that the mean field description is not capable of governing the details of the fluctuation measurements. The value we find for ν is larger than its mean field equivalent, which means $\tau_a\Omega$ decreases faster with Γ^* than it does in a mean field system. The deviation in the value for ν suggests that the slow and the fast flowing branches are, compared to a mean field system, relatively stable close to Γ_c. This is a useful observation towards precisely understanding the two flowing states.

The second step in investigating the scaling of $\tau_a\Omega$ and σ_ω/Ω is to consider their complete scaling with Γ^* *and* T^*, rather than only approaching the critical point via the inflection points of the flow curves. To achieve this we try to find a scaling function of the form [112]:

$$\Omega\tau_a \text{ or } \sigma_\omega/\Omega = \frac{1}{\Gamma^{*\Delta}}\mathscr{F}\left(\frac{T^{*\gamma}}{\Gamma^*}\right) , \tag{4.22}$$

however, due to a limited amount of data (very close to the critical point), uncertainty in the value of Γ_c, and an asymmetry between slow and fast flow (even though the scaling could in principle be different on both sides of the transition), we are unable to find such a scaling relation.

Conclusion – In this section we have shown that we can extract robust values for the magnitude and time scale of the fluctuations in the stress-controlled experiments. The scaling of the magnitude agrees with the scaling of the slope at the inflection point of the flow curves and the corresponding mean field exponent. The exponent that we find for the scaling of the time scale is larger than its mean field equivalent. This suggests that the average quantities in our system do agree with a mean field description, whereas the fluctuations show deviations. This, in turn, is a reflection of the differences between the slow and fast flowing states in our system and the states in mean field systems.

4.A Appendix

4.A.1 Collective Behavior

A fundamental property of a second-order critical point is collective behavior of the particles, which arises in the correlation length ξ. We have searched for this in two different ways.

First, we have studied the location and width (and their fluctuations) of the shear band, as well as the precession of the core for varying T and Γ. We found that the flow structure is actually very robust, with an only exception for the moving shear band for high Γ and small Ω (see Sec. 3.4.3), which we believe is not related to our critical point.

Second, we have looked at so-called kymographs of pictures of the surface of the system. For this, we identify a circular path on the surface that the particles follow. We then make a 2D picture where each horizontal line corresponds to the same image line, but a different moment in time. This way, the trajectories of all the particles on the identified path are visualized. We took kymographs close and far from the critical point in (T, Γ)-space, but found no significant differences.

Of course, our system is relatively small (the shear band is only a few particle wide), the particles are incompressible, and we can only observe what happens at the surface. Therefore, not only is it physically hard to imagine a certain blob of particles moving at a different speed than the adjacent blobs, even if it does happen, it would be hard to observe [113].

4.A.2 T-Control Flow Curves

In Sec. 4.4 we discussed flow curves that were measured in Ω-control. To look at the transition between slow and fast flow from a different perspective, we measure an additional set of flow curves in T-control and plot them on a double linear scale.

The data is presented in Fig. 4.25. In (a), we first plot the $\Omega(T)$ flow curves in the usual logarithmic Ω-axis representation, and see that they are of similar shape as the curves that are measured in rate control (note that the T and Ω axis are interchanged compared to our usual Ω-control plots such as Fig. 4.1). The main difference is the absence of the negative slope, which is replaced by a discontinuous jump in the data for $\Gamma < \Gamma_c$.

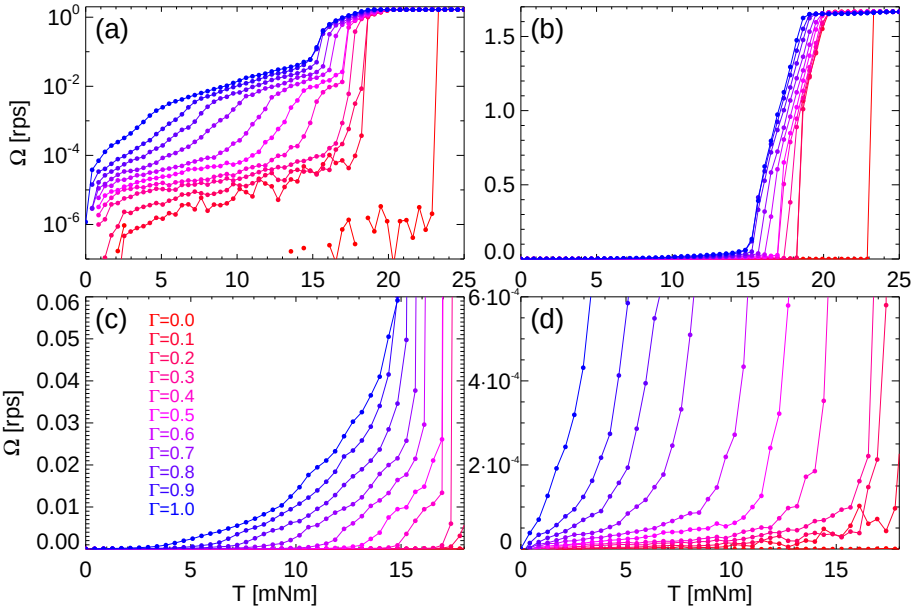

FIGURE 4.25: Flow curves measured in T-control plotted on log-lin (a) and lin-lin (b-d), where (c-d) are zoom ins of (b). The curves are bounded by $\Omega = 1.66$ rps which is the maximum rotation rate of the rheometer. The different flow regimes that we can identify using this representation are discussed in App. 4.A.3.

The curves are bounded by $\Omega = 1.66$ rps, which is the maximum rotation rate of the rheometer.

In panels (b-d) we plot the data in a lin-lin representation. In (b), we see the fast flow regime where Ω grows linearly with T. The curves are parallel to each other, which indicates that the flow rate is mostly determined by the stress, where the vibrations are just a small correction. In (c-d), we zoom in to the slow flow regime. For very small T, $\Omega(T)$ seems linear, and above a certain "kink", it increases exponentially. In App. 4.A.3 we will use these observations as ingredients towards finding a simple model to describe the flow of weakly vibrated granular media.

4.A.3 Towards a Simple Model

We want to see if we can introduce a simple heuristic model similar to those of Bocquet *et al.* [114–116], Kamrin *et al.* [68–70], and Kuwano *et al.* [87] to describe the transition from slow to fast flow. The key ingredient of this model is that we consider the granular system from the point of fluidity, which is a result of both the vibration and the flow itself.

In flow curves such as the ones in Fig. 4.25, we can identify four different regimes. *(i)* For finite Γ and very low Ω, $\Omega(T)$ is linear. We interpret this by saying that the vibrations fluidize the grains to become a very viscous liquid-like material where stable, slow flow is possible. *(ii)* For faster rates, $\Omega(T)$ becomes curved upwards, where a higher flow rate requires a relatively small increase in T. This is, we believe, due to self-fluidization caused by the flow itself. The flow makes the system more fluid, so at similar T, it can now flow faster. *(iii)* For $\Gamma^* < 0$, there is a jump in stress-controlled, and a negative slope in rate-controlled experiments. This is perhaps the hardest regime to understand. Apparently, there is a Γ-dependent "yield" torque above which the system jumps to the inertial regime. In rate control, we *can* access these "forbidden" speeds that correspond to the jump. However, we know that there is no constant T which leads to an Ω in this regime, so T *has* to fluctuate. Here, the fluidity picture offers an explanation for the negative slope. In the case of a relative slow, forbidden, Ω, the rheometer often has to impose a large T to rebreak the contacts to allow for a forbidden rate. For a relatively fast, but forbidden, Ω, the system is very fluid, so the fluctuations to large T (to sustain the flow) can be smaller. For $\Gamma^* > 0$, regime *(iii)* does not exist, and the self-fluidizing regime *(ii)* is directly connected to the inertial flow branch. *(iv)* In the inertial regime [90], $\Omega(T)$ is linear, but the relation does not cross the origin. We explain this as follows: the T splits into two contributions, one to completely break the contacts and one to sustain the fast flow. In this regime, $T(\Omega)$ still depends on Γ. We believe this is because, at higher Γ, a smaller portion of T is required to break the contacts, so more T is left to reach a higher flow rate.

We hope to concretize this concept either by finding analytic expressions for $T(\Omega, \Gamma)$ and $\Omega(T, \Gamma)$, or by developing an iterative simulation that, for each time step, compares T with the current fluidity, and adapts the rate accordingly.